Closure Schemes for Stably Stratified Atmospheric Flows without Turbulence Cutoff

Li, Dan

2016-12

Li , D , Katul , G G & Zilitinkevich , S S 2016 , ' Closure Schemes for Stably Stratified Atmospheric Flows without Turbulence Cutoff ' , Journal of the Atmospheric Sciences , vol. 73 , no. 12 , pp. 4817-4832 . https://doi.org/10.1175/JAS-D-16-0101.1

http://hdl.handle.net/10138/224162
https://doi.org/10.1175/JAS-D-16-0101.1

publishedVersion

Closure Schemes for Stably Stratified Atmospheric Flows without Turbulence Cutoff

DAN LI

Department of Earth and Environment, Boston University, Boston, Massachusetts

GABRIEL G. KATUL

Nicholas School of the Environment, and Department of Civil and Environmental Engineering, Duke University, Durham, North Carolina

SERGEJ S. ZILITINKEVICH

Finnish Meteorological Institute, and Division of Atmospheric Sciences, University of Helsinki, Helsinki, Finland, and Department of Radio Physics, N.I. Lobachevski State University of Nizhniy Novgorod, Nizhniy Novgorod, and Faculty of Geography, Moscow University, and Institute of Geography, Russian Academy of Sciences, Moscow, Russia, and Nansen Environmental and Remote Sensing Center/Bjerknes Centre for Climate Research, Bergen, Norway

(Manuscript received 30 March 2016, in final form 21 August 2016)

ABSTRACT

Two recently proposed turbulence closure schemes are compared against the conventional Mellor–Yamada (MY) model for stably stratified atmospheric flows. The Energy- and Flux-Budget (EFB) approach solves the budgets of turbulent momentum and heat fluxes and turbulent kinetic and potential energies. The Cospectral Budget (CSB) approach is formulated in wavenumber space and integrated across all turbulent scales to obtain flow variables in physical space. Unlike the MY model, which is subject to a "critical gradient Richardson number," both EFB and CSB models allow turbulence to exist at any gradient Richardson number R_i and predict a saturation of flux Richardson number ($R_f \rightarrow R_{fm}$) at sufficiently large R_i. The CSB approach further predicts the value of R_{fm} and reveals a unique expression linking the Rotta and von Kármán constants. Hence, all constants in the CSB model are nontunable and stability independent. All models agree that the dimensionless sensible heat flux decays with increasing R_i. However, the decay rate and subsequent cutoff in the MY model appear abrupt. The MY model further exhibits an abrupt cutoff in the turbulent stress normalized by vertical velocity variance, while the CSB and EFB models display increasing trends. The EFB model produces a rapid increase in the ratio of turbulent potential energy and vertical velocity variance as R_{fm} is approached, suggesting a strong self-preservation mechanism. Vertical anisotropy in the turbulent kinetic energy is parameterized in different ways in MY and EFB, but this consideration is not required in CSB. Differences between EFB and CSB model predictions originate from how the vertical anisotropy is specified in the EFB model.

1. Introduction

Few dispute the claim that turbulence parameterization in stably stratified atmospheric flows remains a daunting task (Fernando 1991; Derbyshire 1999; Mahrt 1999; Basu et al. 2006, 2010; Sorbjan 2006, 2010; Fernando and Weil 2010; Holtslag et al. 2013; Mahrt 2014). Many numerical weather and climate models still employ first-order closure schemes (Huang et al. 2013; Sandu et al. 2013; Karimpour and Venayagamoorthy 2014; Sorbjan 2014) that link turbulent fluxes of momentum and heat to the mean gradients of longitudinal velocity and temperature using turbulent viscosity for momentum K_m and turbulent diffusivity for heat K_h, despite the fact that second-order (and higher-order) closure schemes such as the Mellor–Yamada model (Mellor and Yamada 1974, 1982) and its variants

Corresponding author address: Dan Li, Department of Earth and Environment, Boston University, 685 Commonwealth Ave., Boston, MA 02215.
E-mail: lidan@bu.edu

DOI: 10.1175/JAS-D-16-0101.1

(Galperin et al. 1988) have been proposed for geophysical flows decades ago. One of the challenges associated with applying second-order or higher-order closure schemes to geophysical flows is the buoyancy effect (e.g., due to temperature stratification in the atmosphere), which adds governing equations (e.g., those for sensible heat flux and temperature variance) and concomitantly more empirical constants to the system. For example, the level-2 Mellor–Yamada model requires five (Mellor 1973) or seven (Yamada 1975) constants to be empirically determined, many of which arise from the Rotta closure (Rotta 1951a,b) for pressure–velocity and pressure–temperature correlations and relations between different mixing lengths and a ''master'' length scale. Other second-order Mellor–Yamada type models (Nakanish 2001; Cheng et al. 2002) formulate parameterizations for pressure–velocity and pressure–temperature correlations that go beyond the linear Rotta term and first-order corrections to it at the expense of additional empirical constants. Besides the number of constants, second-order closure schemes have other issues, especially for stable atmospheric conditions. For example, the level-2 Mellor–Yamada (MY) model predicts a so-called critical gradient Richardson number (0.2–0.3) above which the flow is presumed to laminarize and turbulent fluxes are presumed to vanish. Such prediction is not supported by observational (Galperin et al. 2007) and numerical (Gerz et al. 1989; Kosovic and Curry 2000) evidence and has motivated further developments in closure schemes (Cheng et al. 2002; Zilitinkevich et al. 2007; Canuto et al. 2008; Ferrero et al. 2011) that rectify such issues.

Two recent developments are the Energy- and Flux-Budget (EFB) model (Zilitinkevich et al. 2007, 2008, 2013) and the Cospectral Budget (CSB) model (Katul et al. 2013a, 2014; Li et al. 2015a,b). The EFB solves the turbulent potential energy (TPE) budget, the turbulent kinetic energy (TKE) budget, and the budgets of momentum and heat fluxes in physical space. This model does not require a critical gradient Richardson number. It has been shown that the parameterizations for the pressure–velocity and pressure–temperature correlations, which differ from the widely used Rotta model, are the key to alleviating the need for a critical gradient Richardson number (Canuto et al. 2008). By allowing the relaxation time scale in the Rotta model for the pressure–temperature correlation to be atmospheric stability dependent, the MY-type closure schemes can also allow turbulence to exist beyond the critical gradient Richardson number (Canuto et al. 2008; Ferrero et al. 2011). The EFB scheme, however, does not reduce appreciably the number of constants to be specified when compared to the MY model.

Recent linkages between the mean velocity and temperature profiles and the shapes of turbulent energy spectra provide an alternative to predicting the bulk flow properties and determining closure constants. The CSB model achieves such a link by solving two cospectral budget equations of momentum and heat fluxes based on assumed spectral shapes of the turbulent vertical velocity and air temperature. The premise in CSB is that small scales may reasonably follow well-known inertial subrange scaling laws, and the presence of a boundary tends to randomize the energy content of large scales. Unlike the other closure schemes, this model is framed in spectral space and links the cospectra of momentum and heat to mean gradients and energy spectra. By integrating over all turbulent scales, the CSB model connects turbulent fluxes to mean gradients and the energetics of the flow (potential and kinetic) in physical space.

Given all these separate developments, the time is now ripe to examine similarities and differences between the EFB and CSB models in relation to well-established closure schemes, such as the MY model. This exploration is motivated by a recent study that reported acceptable agreement between the EFB and CSB models in capturing the turbulent Prandtl number with increasing Richardson number under stable conditions (Li et al. 2015b). However, such agreement in isolation may be deemed insufficient given the possible self-correlation arising from common variables affecting the turbulent Prandtl and Richardson numbers (Klipp and Mahrt 2004; Esau and Grachev 2007; Grachev et al. 2007; Anderson 2009; Rodrigo and Anderson 2013). Hence, the work here examines a manifold of connections between turbulent stresses, turbulent heat fluxes, the vertical velocity variance, the temperature variance, and atmospheric stability changes across all three models for stable stratification. Such comparisons between ordinary and spectral closures are expected to shed new light on how to constrain closure constants and offer a new perspective on future model developments. As a logical starting point, the focus is on the idealized stationary and planar homogeneous atmospheric surface layer flow at sufficiently large Reynolds numbers under mildly to moderately stable conditions. Such idealized atmospheric surface layer turbulence is selected here so as to highlight the effects of different physics behind the aforementioned closure schemes on flow predictions. It is envisaged that the findings here may benefit future closure parameterization of stably stratified turbulent flows in large-scale weather and climate models. Cases where turbulence becomes globally intermittent or nonstationary and cases where atmospheric stability is sufficiently large to admit gravity waves are outside the scope of this work.

2. Theory

In this study, a dry, stably stratified atmospheric surface layer flow is considered. The stability effects are represented by the gradient R_i and flux R_f Richardson numbers defined as follows:

$$R_i = \frac{\beta\Gamma}{S^2} = \frac{N^2}{S^2} \quad \text{and} \tag{1}$$

$$R_f = -\frac{\beta\overline{w'\theta'}}{-S\overline{u'w'}} = \frac{\beta}{S}\frac{\int_0^\infty F_{wT}(k)\,dk}{\int_0^\infty F_{uw}(k)\,dk}, \tag{2}$$

where the overline denotes Reynolds averaging and primes denote turbulent fluctuations from the averaged state, $\beta = g/\overline{\theta}$ is the buoyancy parameter, g is the gravitational acceleration constant, θ is the potential temperature, $\Gamma = \partial\overline{\theta}(z)/\partial z$ is the mean air temperature gradient, $N = (\beta\Gamma)^{1/2}$ is the Brunt–Väisälä frequency, $S = \partial\overline{u}(z)/\partial z$ is the mean velocity gradient, u is the longitudinal velocity, w is the vertical velocity, $\tau = -\rho\overline{u'w'} > 0$ is the turbulent momentum flux (without loss of generality, the coordinate system is oriented so that the mean lateral velocity $\overline{V} = 0$ and $\overline{v'w'} \approx 0$), ρ is the mean air density, $F_z = \overline{w'\theta'}$ is the kinematic sensible heat flux (<0 for stable conditions), $-S\overline{u'w'}$ is the mechanical production rate of TKE, $\beta\overline{w'\theta'}$ is the buoyancy destruction rate of TKE, and $F_{uw}(k)$ and $F_{wT}(k)$ are the momentum flux and heat flux cospectra at wavenumber k, which is interpreted here as the wavenumber in the longitudinal direction for consistency with field studies in the atmospheric surface layer (Kaimal and Finnigan 1994). These definitions result in a turbulent Prandtl number given by $\mathrm{Pr}_t = R_i/R_f$.

The governing equations and key assumptions employed by all three modeling approaches are presented in the appendix and are not repeated here. Six nondimensional variables are considered for model comparisons, including the flux Richardson number, the turbulent Prandtl number, the momentum flux, the sensible heat flux, the ratio of temperature and vertical velocity variances, and the vertical anisotropy, defined as the ratio of the vertical component of TKE and the total TKE.

a. The MY model

The MY model includes a hierarchy of closure schemes, and the level-2 scheme is considered, given its quasi-analytical tractability. The final result of Yamada (1975) is used here, which requires the determination of seven basic constants, including three for the Rotta model (C_1, C_2, and C_3) and four for length scale proportionality to the master length scale for various terms (A_1, A_2, B_1, and B_2).

The turbulent Prandtl number from the MY model for atmospheric surface layer flows is

$$\frac{\mathrm{Pr}_t^{-1}}{\mathrm{Pr}_{t,\mathrm{neu}}^{-1}} = \frac{1 - R_f/R_{f,2}}{1 - R_f/R_{f,1}}, \tag{3}$$

where $\mathrm{Pr}_{t,\mathrm{neu}}^{-1} = (C_H R_{f,2})/(C_M R_{f,1})$ is the inverse of the turbulent Prandtl number under neutral conditions. Here, $C_H = 1.978$, $C_M = 1.436$, $R_{f,1} = 0.325$, and $R_{f,2} = 0.316$ are constants derived from the seven basic constants earlier discussed. As a result, $\mathrm{Pr}_{t,\mathrm{neu}} = 0.74$. Given Eq. (3) and $\mathrm{Pr}_t = R_i/R_f$,

$$R_i = R_f \frac{C_M R_{f,1}}{C_H R_{f,2}} \frac{1 - R_f/R_{f,1}}{1 - R_f/R_{f,2}}, \tag{4}$$

which allows the determination of the maximum flux Richardson number across a range of R_i occurring in nature. This "maximum flux Richardson number" is also termed the "critical Richardson number" in Yamada (1975). To distinguish this term from the "critical gradient Richardson number" historically used to indicate laminarization of turbulent flows for very stable conditions, the term "maximum flux Richardson number" is used throughout and is referred to as R_{fm}.

The sensible heat flux F_z (<0 for stable conditions) is determined as follows:

$$\frac{F_z^2}{e_w e_T} = \frac{C_H}{0.25 B_2} \frac{(R_{\mathrm{fm}} - R_f)}{1 - R_f} \frac{1}{A_z}, \tag{5}$$

where $B_2 = 8$ is one of the basic empirical constants, $e_w = (1/2)\overline{w'^2}$ is the vertical component of TKE, and $e_T = (1/2)\overline{\theta'^2}$ is half of the temperature variance. Note such normalized sensible heat flux is similar to the correlation coefficient between vertical velocity and temperature fluctuations. The vertical anisotropy, or the fraction of TKE in the vertical direction A_z, is given by

$$A_z = \frac{e_w}{e} = \frac{1}{3} - 2\frac{A_1}{B_1} - 6\frac{A_1}{B_1}\left(1 - \frac{2}{3}C_2\right)\frac{R_f}{1 - R_f}, \tag{6}$$

where e is the total TKE, and $A_1 = 0.78$, $B_1 = 15$, and $C_2 = 0.3$ are three other basic empirical constants in the MY model. The momentum flux τ is calculated through

$$\left(\frac{\tau}{e_w}\right)^2 = \frac{1}{0.25 B_1}\frac{S_m}{A_z^2}\frac{1}{1 - R_f}, \tag{7}$$

where

$$S_m = C_M \frac{(R_{\rm fm} - R_f)(R_{f,1} - R_f)}{(1 - R_f)(R_{f,2} - R_f)}. \quad (8)$$

The ratio of temperature variance and vertical velocity variance, or the ratio of TPE and the vertical component of TKE where TPE (represented by e_p) is defined as $e_p = (\beta/N)^2 e_T$, can be determined by

$$\frac{e_p}{e_w} = \frac{B_2}{B_1}\frac{1}{A_z}\frac{R_f}{1 - R_f}. \quad (9)$$

Evident from Eq. (9) is that, as stability (or R_f) increases, the ratio of e_p to e_w increases. It can be also seen that the ratio e_p/e_w is amplified by the stability dependence of A_z (usually A_z decreases with increasing R_f), while the ratio $e_p/e = (B_2/B_1)R_f/(1 - R_f)$ is independent of A_z. These expressions are compared to predictions from the EFB and CSB models described next.

b. The EFB model

The EFB model, proposed by Zilitinkevich et al. (2007, 2008, 2013), uses a set of budget equations for the second-order moments: namely, equations for momentum flux, sensible heat flux, TKE, and TPE. The EFB model recognizes and quantifies the negative feedback between TKE and TPE that prevents turbulence from degenerating under strongly stratified turbulence (a mechanism labeled as self-preservation). The negative buoyancy flux converts part of the TKE into TPE and thus decreases TKE and increases TPE [see Eqs. (A4) and (A6)]. As a result, the increased TPE generates positive contributions to the buoyancy flux [Eq. (A2)] and hence weakens the total negative buoyancy flux, which further results in reestablishing TKE and prevents degeneration or collapse of turbulence.

Results from the most recent version of the EFB model (Zilitinkevich et al. 2013) are used here. The turbulent Prandtl number is given by

$$\frac{{\rm Pr}_t^{-1}}{{\rm Pr}_{t,\rm neu}^{-1}} = 1 - \frac{R_f}{1 - R_f}\frac{(1 - R_{\rm fm})}{R_{\rm fm}}\frac{A_z^\infty}{A_z}, \quad (10)$$

where ${\rm Pr}_{t,\rm neu}^{-1} = C_\tau^{\rm efb}/C_F^{\rm efb}$ is the inverse turbulent Prandtl number under neutral conditions. The constants $C_\tau^{\rm efb}$ and $C_F^{\rm efb}$ are the dissipation time scales for momentum and heat fluxes, the values of which are empirically determined as 0.1 and 0.125, respectively.[1] The $R_{\rm fm}$ is again the maximum flux Richardson number resulting from the feedback between the TKE and TPE budgets as well as the heat flux budget (Zilitinkevich et al. 2013). This $R_{\rm fm}$ is determined from observations (=0.25) in the EFB model. The A_z is given by

$$A_z = \frac{C_r^{\rm efb}\left(1 - 2C_o^{\rm efb}\dfrac{R_f}{R_{\rm fm}}\right)(1 - R_f) - 3R_f}{(1 - R_f)\left\{3 + C_r^{\rm efb}\left[3 - 2(1 + C_o^{\rm efb})\dfrac{R_f}{R_{\rm fm}}\right]\right\}}, \quad (11)$$

where $C_r^{\rm efb}$ (=1.5) is a standard intercomponent energy exchange constant, and $C_o^{\rm efb}$ (=0.125) is the intercomponent energy exchange constant determining the vertical share of TKE. The constant A_z^∞ (=0.03) is the value of A_z at $R_i \to \infty$, which can be determined from the other basic constants. Given Eq. (10) and ${\rm Pr}_t = R_i/R_f$,

$$R_i = R_f \frac{C_\tau^{\rm efb}}{C_F^{\rm efb}}\left[1 - \frac{R_f}{1 - R_f}\frac{(1 - R_{\rm fm})}{R_{\rm fm}}\frac{A_z^\infty}{A_z}\right]. \quad (12)$$

The sensible heat F_z and momentum τ fluxes can be determined as follows:

$$\frac{F_z^2}{e_w e_T} = \frac{2C_\tau^{\rm efb}}{C_P^{\rm efb}}\frac{1}{{\rm Pr}_t} \quad \text{and} \quad (13)$$

$$\left(\frac{\tau}{e_w}\right)^2 = \frac{2C_\tau^{\rm efb}}{A_z}\frac{1}{1 - R_f}, \quad (14)$$

where $C_P^{\rm efb}$ is the dissipation time-scale constant for TPE (=0.417). The ratio of e_p to e_w, which represents the ratio of TPE to TKE in the vertical direction, is given as

$$\frac{e_p}{e_w} = \frac{C_P^{\rm efb}}{A_z}\frac{R_f}{1 - R_f}. \quad (15)$$

Equation (15) suggests that, as atmospheric stability increases, the ratio of e_p to e_w increases, which is consistent with the self-preservation mechanism mentioned earlier. Similar to the MY model, the ratio of $e_p/e = C_P^{\rm efb}R_f/(1 - R_f)$ in the EFB model is also independent of A_z.

c. The CSB model

The CSB approach differs from ordinary turbulence closure schemes such as the MY and EFB models, as it solves the cospectral budgets for momentum and heat fluxes in spectral space and then integrates across all wavenumbers to arrive at macroscopic results in physical space (Katul et al. 2014). The key input is idealized

[1] The values of $C_\tau^{\rm efb}$, $C_F^{\rm efb}$, and $C_P^{\rm efb}$ in Eq. (13) are slightly different from those used in Zilitinkevich et al. (2013) because of a typing error when determining $C_\tau^{\rm efb}$ and $C_P^{\rm efb}$ in Zilitinkevich et al. (2013).

spectral shapes for the vertical velocity and air temperature, which are principally based on the Kolmogorov (Kolmogorov 1941a,b) and the Kolmogorov–Obukhov–Corrsin (Corrsin 1951; Obukhov 1968) scaling, respectively, at small scales.

For the turbulent Prandtl number normalized by its value in neutral conditions, the CSB model predicts

$$\frac{\mathrm{Pr}_t^{-1}}{\mathrm{Pr}_{t,\mathrm{neu}}^{-1}} = 1 - \frac{R_f}{1-R_f}\frac{1}{1-C_{\mathrm{IT}}}\frac{C_T}{C_o}, \tag{16}$$

where

$$\mathrm{Pr}_{t,\mathrm{neu}}^{-1} = \frac{A_T(1-C_{\mathrm{IU}})}{A_u(1-C_{\mathrm{IT}})}. \tag{17}$$

The constants C_o and C_T are the Kolmogorov and Kolmogorov–Obukhov–Corrsin constants for the vertical velocity and temperature spectra in the inertial subrange, respectively. For a one-dimensional wavenumber interpretation of k along the longitudinal direction, their values are $C_o = 0.65$ and $C_T = 0.8$ (Ishihara et al. 2002; Chung and Matheou 2012). The A_u, A_T, C_{IU}, and C_{IT} originate from the Rotta model in spectral space. In particular, C_{IU} and C_{IT} are constants associated with isotropization of production terms whose value ($\approx$3/5) can be determined using rapid distortion theory in homogeneous turbulence (Pope 2000). The CSB model further shows that the basic Rotta constants A_u and A_T are related to the von Kármán constant κ, C_o, and C_{IU} through (Katul et al. 2013b, 2014):

$$\left(\frac{7}{4}\frac{1-C_{\mathrm{IU}}}{A_u}C_o\right)^{3/4} = \kappa. \tag{18}$$

Although it appears that the CSB model requires six constants (C_o, C_T, A_u, A_T, C_{IU}, and C_{IT}), all of them are well constrained. The Kolmogorov constant C_o and the Kolmogorov–Obukvov–Corrsin constant C_T are well established and do not vary with boundary conditions or stability. The isotropization of production constants C_{IU} and C_{IT} have been predicted from other theories and are not expected to vary with stability. Equation (18) provides a constraint on the Rotta constant A_u (and a similar constraint exists for A_T), which is assumed here not to vary with stability. Variations of A_u with stability, if they exist, must be accompanied by canceling variations in $1 - C_{\mathrm{IU}}$ to maintain the von Kármán constant independent of stability. As a result, the CSB model does not require a priori constant specification, as all the constants are general to turbulence and do not vary with stability. The limiting assumptions remain the shapes of the air temperature and vertical velocity spectra at large scales.

The CSB predicts F_z and τ by integrating across all wavenumbers of the modeled cospectra to yield

$$\frac{F_z^2}{e_w e_T} = \frac{28}{25}\left(\frac{1-C_{\mathrm{IU}}}{A_u}\right)C_T^{-1}\frac{1}{\mathrm{Pr}_t} \quad \text{and} \tag{19}$$

$$\left(\frac{\tau}{e_w}\right)^2 = \frac{28}{25}\left(\frac{1-C_{\mathrm{IU}}}{A_u}\right)C_o^{-1}\frac{1}{1-R_f}. \tag{20}$$

With Eq. (18), they can be rewritten as follows:

$$\frac{F_z^2}{e_w e_T} = \frac{16}{25}\kappa^{4/3}C_o^{-1}C_T^{-1}\frac{1}{\mathrm{Pr}_t} \quad \text{and} \tag{21}$$

$$\left(\frac{\tau}{e_w}\right)^2 = \frac{16}{25}\kappa^{4/3}C_o^{-2}\frac{1}{1-R_f}. \tag{22}$$

Further assuming equilibrium in e and half-temperature variance budgets, as in the MY model, yields

$$\frac{e_p}{e_w} = \frac{C_T}{C_o}\frac{R_f}{1-R_f}. \tag{23}$$

3. Results

Figure 1 compares the three models in terms of the relation between R_f and R_i (left panels) and the relation between Pr_t and R_i (right panels). The top panels are results from the three models (for clarity), while the bottom panels include experiments and simulations. The EFB and CSB models produce comparable results, and both capture the main features, such as the saturation of R_f and the linear increase in Pr_t at sufficiently large R_i, which have been observed before (Zilitinkevich et al. 2013; Li et al. 2015b). However, other field experiments found rapid decrease of R_f for $R_i > 1$ (Pardyjak et al. 2002), which is not predicted here. Both models also predict persistence of turbulence at any R_i and do not support the concept of critical gradient Richardson number. In essence, the EFB model argues that R_i depends only on the mean flow state, and increases in R_i are not limited by the internal turbulence state (i.e., the ability of turbulence to transport momentum and heat). The CSB model implicitly employs this argument and treats the vertical gradients of mean velocity and temperature as "external" variables to the cospectral budgets. By virtue of this treatment, the CSB model is also not limited by a critical gradient Richardson number. The MY model nonetheless differs from the EFB and CSB models. It yields a critical gradient Richardson number that is about 0.25. Beyond this value, R_f and Pr_t no longer change with increasing R_i. Although the saturation of the flux Richardson number when the

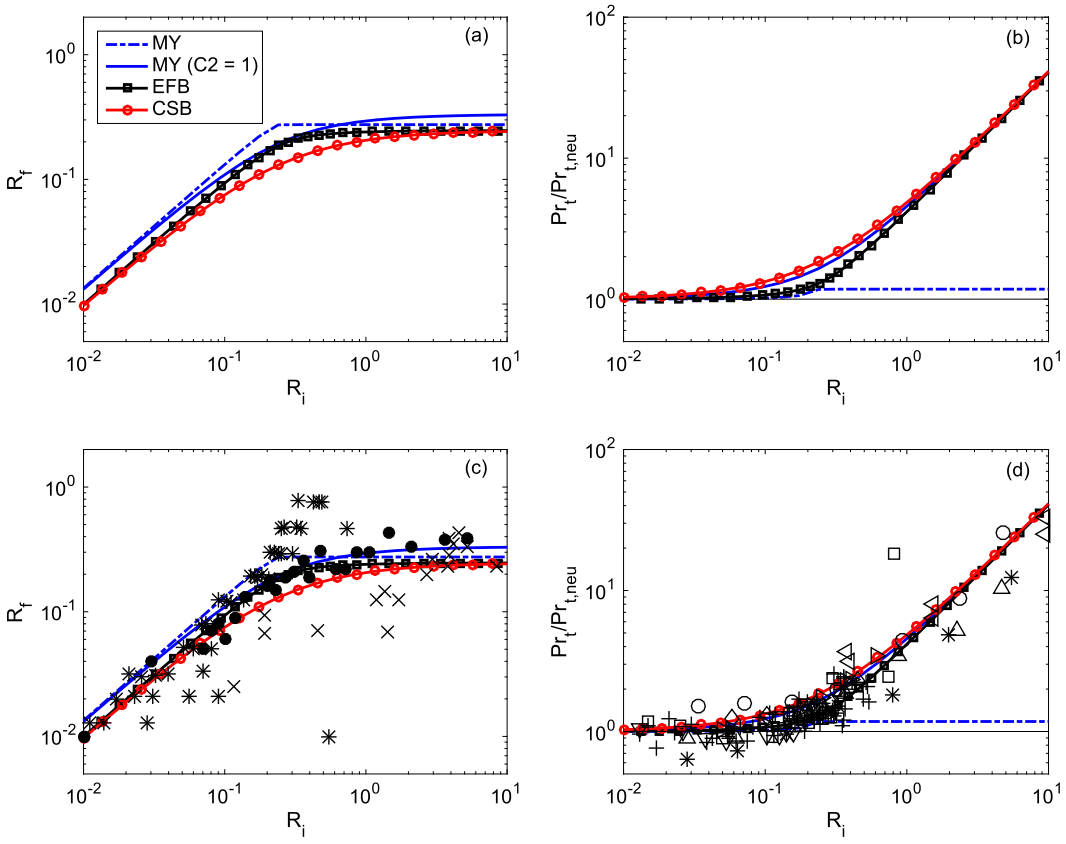

FIG. 1. (a) The flux Richardson number R_f and (b) the turbulent Prandtl number $\mathrm{Pr}_t/\mathrm{Pr}_{t,\mathrm{neu}}$ as functions of gradient Richardson number R_i. (c),(d) As in (a),(b), but data and other simulations are added for reference. Data are from numerical simulations, including direct numerical simulations (DNS) and large-eddy simulations (LES), and laboratory and field experiments, denoted by the following symbols: ∗ SHEBA field experiment (Grachev et al. 2007), × laboratory (Strang and Fernando 2001), • LES (Nakanish 2001), ▷ DNS (Shih et al. 2000), ◁ DNS (Stretch et al. 2010), ▽ DNS (Chung and Matheou 2012), △ LES (Esau and Grachev 2007), ◇ LES (Andren 1995), + water channel (Rohr et al. 1988), □ wind tunnel (Webster 1964), and ○ wind tunnel (Ohya 2001). The SHEBA data shown in (c) are for $R_f < 1$ (i.e., finite TKE dissipation rate). The black thin line in (b) and (d) indicates a value of 1.

gradient Richardson number exceeds the critical value is reasonably supported by observations, the turbulent Prandtl number from the MY model is not congruent with the many experiments. The existence of a critical gradient Richardson number is a topic that continues to receive attention in turbulence modeling (Canuto et al. 2008; Ferrero et al. 2011), but experimental evidence favors no such threshold (Galperin et al. 2007).

Two important caveats should be highlighted here. First, the calculations of R_i, R_f, and Pr_t from data, especially those from field experiments, are not free from large uncertainties. At any given R_i, the scatter in computed Pr_t may span nearly a decade (Grachev et al. 2007, 2012; Li et al. 2016). The data shown in Fig. 1 from the SHEBA field experiment are actually the bin-averaged Pr_t. The large scatter associated with the Pr_t–R_i relation is partly due to the fact that the vertical gradients of mean velocity and air temperature are difficult to resolve, given that the measurement heights are in close proximity, thereby amplifying random errors due to sensor resolution. Second, the Pr_t–R_i relation suffers from self-correlation as both Pr_t and R_i require the vertical gradients of velocity and air temperature, the variations of which tend to lead to Pr_t that artificially increases with increasing R_i (Klipp and Mahrt 2004; Esau and Grachev 2007; Grachev et al. 2007; Anderson 2009; Rodrigo and Anderson 2013). However, the acceptable R_i–R_f agreement between models and with data can be used as indirect evidence that the Pr_t–R_i relation is a robust outcome, given that the R_i–R_f comparison does not suffer from the aforementioned self-correlation issue.

As in Canuto et al. (2008), the question of whether the traditional MY model can encompass an arbitrary large R_i and what changes to the MY model are needed to allow it to do so is explored. Based on the model

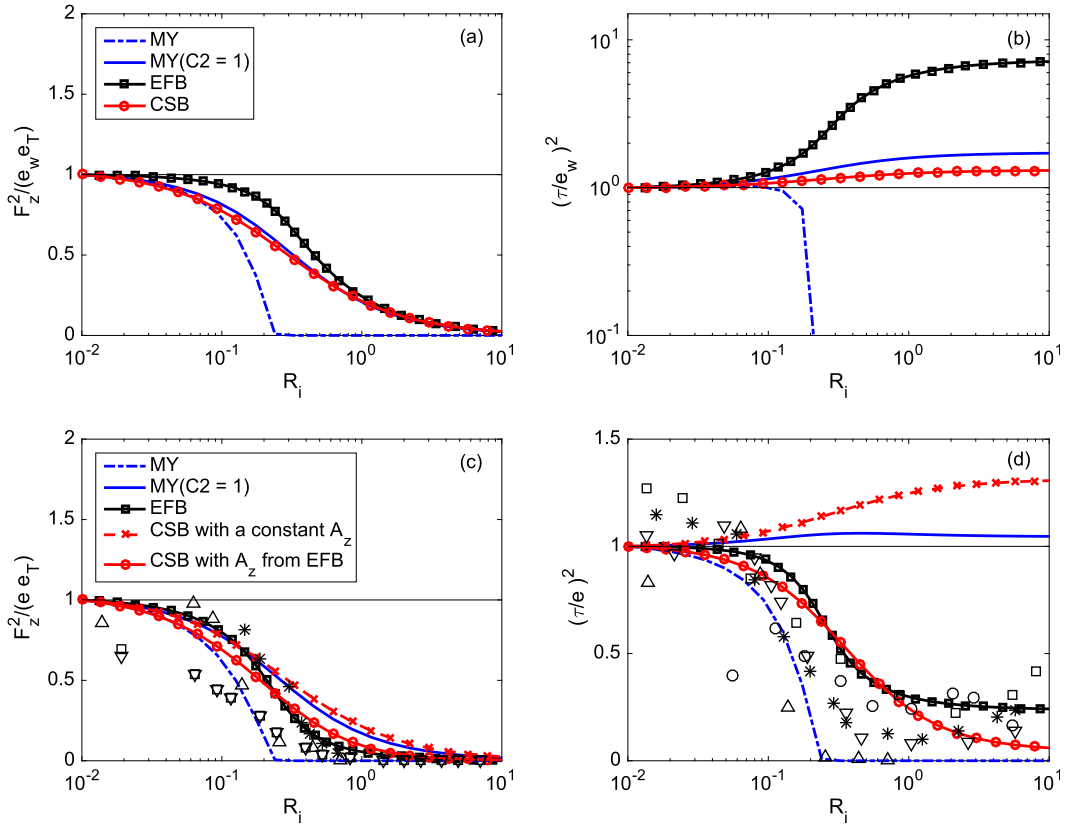

FIG. 2. (a),(c) The normalized sensible heat flux F_z and (b),(d) the normalized momentum flux τ as a function of the gradient Richardson number R_i; (a) and (b) use e_w, while (c) and (d) use e as the normalization factor. The ordinate is further normalized by the model neutral values to adjust for some differences in near-neutral states. The black thin line indicates a value of 1. Symbols denote data sources as follows: ∗ SHEBA field experiment Grachev et al. (2007), △ LES [provided by Igor Esau as in Zilitinkevich et al. (2007)], □ Carbon in the Mountains Experiment (Mahrt and Vickers 2005), ▽ Cooperative Atmosphere–Surface Exchange Study (Poulos et al. 2002), and ○ wind tunnel (Ohya 2001).

described in Cheng et al. (2002), the study by Canuto et al. (2008) modified the relaxation time scale in the Rotta closure for the pressure–temperature decorrelation to allow it to change with atmospheric stability. An alternative is to modify the value of one of the basic constants in the MY model that appears in the Rotta closure for pressure–velocity decorrelation (C_2) to unity here. The rationale behind this choice of C_2 is that it eliminates the dependence of the turbulent momentum flux on $\overline{u'\theta'}$. In part, this revision is inspired by the CSB approach. When considering the turbulent stress budget in wavenumber space $F_{uw}(k)$, the cospectrum $F_{uT}(k)$ associated with the buoyancy term decays at $-7/3$, while $F_{ww}(k)$ associated with the production term decays only at $-5/3$ with increasing wavenumber k. When carrying out this minor revision to the MY model, the predictions become similar to those from the EFB and CSB models. As can be seen from Fig. 1, increasing C_2 to unity alone allows the MY model to encompass any R_i, and the resulting relation between R_f and R_i and also the relation between Pr_t and R_i become closer to those predicted from the EFB and CSB models. Note that the value of C_2 was also increased from 0.3 in Cheng et al. (2002) to 0.5 in Canuto et al. (2008). However, it should be stressed that, although the MY model can be modified to avoid degeneration of turbulence at large R_i, such modification neither explains the self-preservation mechanism of turbulence nor guarantees its realistic modeling over a wide range of R_i (as shall be seen in Fig. 2). The EFB and CSB models, on the contrary, disclose the key self-preservation mechanism (again, one in the physical domain and the other in the spectral domain): conversion of TKE into TPE by the negative heat flux and self-control of the negative (downgradient) heat flux through the efficient generation of positive (countergradient) heat transfer by TPE.

Despite the agreement on the R_f–R_i–Pr_t relations, Eqs. (10) and (16) reveal fundamental differences

between the EFB and CSB models. The maximum flux Richardson number value is predetermined from observations in the EFB model but is inferred from three phenomenological constants in the CSB model: namely, $C_{\rm IT}$, C_T, and C_o. As demonstrated elsewhere (Katul et al. 2014; Li et al. 2015a), the $R_{\rm fm}$ in the CSB model can be computed as

$$R_{\rm fm} = \frac{1}{1 + \dfrac{1}{1 - C_{\rm IT}} \dfrac{C_T}{C_o}} \approx 0.25, \tag{24}$$

which is consistent with the value used in the EFB model. This illustrates the value of conducting such a comparison between different turbulence closure schemes for constraining empirical constants. Note that experimental studies reported values of R_f larger than $R_{\rm fm} \approx 0.25$ and sometimes even larger than unity. The assumption of equilibrium between shear production, buoyancy destruction, and mean dissipation rate of TKE, which is employed by all models here, does not allow $R_f > 1$. This is why Fig. 1 excluded those data associated with $R_f > 1$ from the SHEBA experiment. Such differences between models and observations again can be attributed to the difficulty in estimating R_f from field experiments, as well as the fact that many features of the stable atmospheric surface layer such as surface heterogeneity (Stoll and Porté-Agel 2009; Miller and Stoll 2013), transients such as passage of clouds (Cava et al. 2004), submeso motions (Mahrt 2009), and gravity waves (Sun et al. 2015; Cava et al. 2015) are not considered here.

Combining Eqs. (16) and (24), the turbulent Prandtl number in the CSB model can also be rewritten as

$$\frac{{\rm Pr}_t^{-1}}{{\rm Pr}_{t,\rm neu}^{-1}} = 1 - \frac{R_f}{1 - R_f} \frac{(1 - R_{\rm fm})}{R_{\rm fm}}. \tag{25}$$

Comparing Eq. (25) to Eq. (10) reveals that the vertical anisotropy A_z is the main difference between the CSB and EFB models for ${\rm Pr}_t$. The factor in the EFB model A_z^{∞}/A_z is close to unity at strong stratification but deviates from unity at weak stratification. However, despite this difference, both models agree in their turbulent Prandtl number predictions across a wide range of stability because the multiplier $R_f/(1 - R_f)$ is small at weak stratification. It is noted here that other empirical formulations for ${\rm Pr}_t$ constructed based on asymptotic behaviors of ${\rm Pr}_t$ and data fitting have been also proposed in previous studies (Schumann and Gerz 1995; Venayagamoorthy and Stretch 2010). Those formulations are different from the formulations of EFB [Eq. (10)] and CSB [Eqs. (16), (24), and (25)] shown here, which are obtained by solving budget equations in the physical and spectral domain, respectively.

Because the normalized squared sensible heat fluxes $[F_z^2/(e_w e_T)]$ are predicted to be proportional to ${\rm Pr}_t^{-1}$ in both EFB and CSB models [see Eqs. (13) and (19)], they appear comparable in Fig. 2a. The original MY model predicts zero sensible heat flux when R_i exceeds the critical value. The modified MY model (i.e., setting $C_2 = 1$) yields similar results to the EFB and CSB models, which is also consistent with Fig. 1. It should be pointed out that here the sensible heat flux is normalized by e_w and e_T, and thus its trend with increasing R_i is different from that of the dimensional quantity, which often displays a negative maximum in the range of $0 < R_i < 0.25$ [e.g., see Fig. 6 in Grachev et al. (2013)].

Figure 2b features the normalized squared momentum fluxes (τ^2/e_w^2). It is first noted that e_w instead of the total TKE (e) is used here to normalize the momentum flux. The rationale is that the production term in the governing equation for momentum flux [Eq. (A1)] only involves the vertical velocity variance. In addition, the CSB model does not require the total TKE, while e_w is predicted in all three models. In the MY [Eq. (7)], EFB [Eq. (14)], and CSB [Eq. (20)] models, τ^2/e_w^2 predictions are all proportional to $1/(1 - R_f)$. The main difference is that τ^2/e_w^2 is principally determined from $1/(1 - R_f)$ in the CSB model [see Eq. (20)], whereas an inverse variation with A_z emerges from the EFB model [see Eq. (14)]. In the MY model [see Eq. (7)], it is inversely proportional to A_z^2 and also proportional to S_m, with both terms changing with R_f. Interestingly, the original MY model suggests that the normalized momentum flux decreases with increasing R_i and vanishes at the critical gradient Richardson number, while the other models (including the modified MY model) suggest that the normalized momentum flux increases with increasing R_i. The increasing rates are the strongest in the EFB model and the weakest in the CSB model. The EFB unambiguously delineates two regimes: strong ($\tau/e_w \sim r_1$ at low R_i) and weak ($\tau/e_w \sim r_2$ at high R_i) momentum transfer, with $r_2/r_1 \sim 5$. The contrast between these two regimes is weaker in the CSB model and the modified MY model (i.e., $1 < r_2/r_1 < 2$) than the one given by the EFB model. This weaker delineation may be attributed to the dependence of e_w on stability that only emerges through the mean dissipation rate of TKE in the CSB model. For reference, the widely used Monin–Obukhov similarity theory often assumes a constant τ/e_w for stably stratified conditions (Stull 1988).

As most reported observations used e instead of e_w as a normalization factor, Figs. 2c and 2d present the model results for $F_z^2/(e e_T)$ and τ^2/e^2, respectively, together with measurements and simulations. Since a

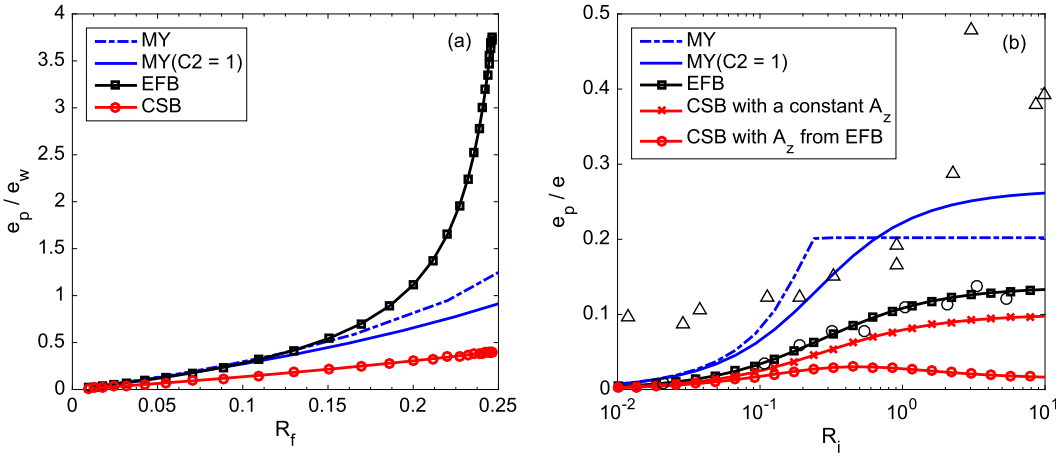

FIG. 3. (a) The ratio of turbulent potential e_p to turbulent kinetic energy in the vertical direction e_w as a function of flux Richardson number R_f. (b) The ratio of turbulent potential e_p to turbulent kinetic energy e as a function of gradient Richardson number R_i. Note that the R_f is restricted by the maximum $R_{\rm fm} \approx 0.25$. Symbols denote data sources as follows: △ LES (Zilitinkevich et al. 2007) and ○ wind tunnel (Ohya 2001).

parameterization for A_z is needed for the CSB model to generate these results, two cases in which the A_z is either set to be a constant (crosses) or taken from the EFB model (circles) are shown. It is clear that τ^2/e^2 is sensitive to A_z when compared to $F_z^2/(eE_T)$. The CSB model runs with the two different parameterizations for A_z show different trends, which highlights the important role of A_z in controlling the normalized momentum flux. The data for $F_z^2/(eE_T)$ have too-large uncertainties to distinguish the performance of different models, except that the original MY model with turbulence cutoff deviates from data in the range of $R_i > 0.2$. On the other hand, Fig. 2d shows that the EFB model and the CSB model with A_z taken from EFB capture the observations for τ^2/e^2 better than the original and modified MY model. It is interesting to point out that the modified MY model, though it does capture the Pr_t–R_i and R_f–R_i relations, predicts a relatively flat (and slightly increasing) trend of τ^2/e^2 with increasing R_i that is inconsistent with data. As a result, the EFB and CSB models outperform the MY model even with a modified C_2 value that avoids turbulence cutoff.

Figure 2 also provides examples that illustrate the linkages between different constants used across different models. For example, the relation between the normalized squared sensible heat flux and R_i involves the ratio of two constants in the EFB model [see Eq. (13)]: namely, $C_\tau^{\rm efb}/C_P^{\rm efb}$. This can be compared to the same relation from the CSB model [see Eq. (21)], yielding

$$\frac{2C_\tau^{\rm efb}}{C_P^{\rm efb}} = \frac{16}{25}\kappa^{4/3}C_o^{-1}C_T^{-1}, \tag{26}$$

which provides a constraint on the value of $C_\tau^{\rm efb}/C_P^{\rm efb}$. Similarly, comparing the relations for normalized momentum flux between EFB and CSB models yields

$$\frac{2C_\tau^{\rm efb}}{A_z(R_i=0)} = \frac{16}{25}\kappa^{4/3}C_o^{-2}. \tag{27}$$

Given the uncertainties in the fitting procedure used to determine $C_\tau^{\rm efb}$, $C_P^{\rm efb}$, and $A_z(R_i = 0)$, these comparisons could provide a new perspective to determining some empirical constants in turbulence closure schemes.

Figure 3a compares e_p/e_w as a function of R_f as predicted by the three models. It can be seen from Eqs. (9), (15), and (23) that e_p/e_w remains proportional to $R_f/(1-R_f)$ in all models. What is different is the proportionality constant, which is $B_2/(B_1A_z)$ in the MY model, $C_P^{\rm efb}/A_z$ in the EFB model, and C_T/C_o in the CSB model. Hence, the main difference is again the vertical anisotropy A_z. In the CSB model, the (e_p/e_w)–R_f relation is fully described by the ratio of the Kolmogorov constant to the Kolmogorov–Obukhov–Corrsin constant. However, the e_p/e_w–R_f relation is impacted by A_z in the MY and EFB models. As shown in Fig. 4, A_z is reduced in the MY and EFB models with increasing stability, and thus the proportionality constants in the MY and EFB models increase with increasing R_f (see Fig. 3a). It should be pointed out that the MY model solves both $\overline{w'w'}$ and the total TKE to obtain A_z, while the EFB model only solves the total TKE but parameterizes A_z.

Figure 3a reflects an important difference between the three models in terms of representing the strength of the self-preservation mechanism. In the EFB model, the ratio e_p/e_w is significantly enhanced when $R_f > 0.1$ as a

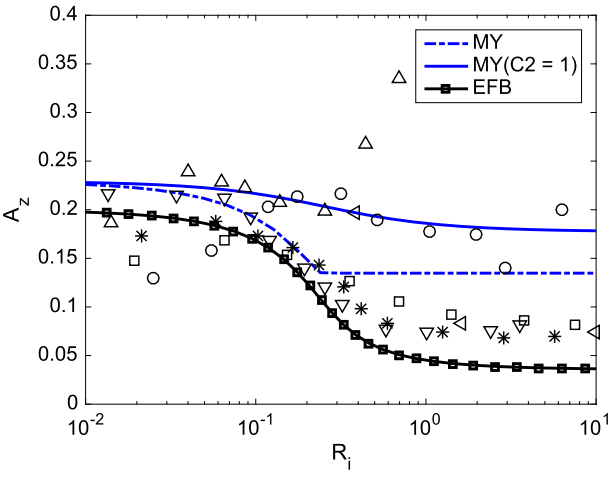

FIG. 4. The vertical anisotropy A_z as a function of gradient Richardson number R_i. Data are from numerical simulations including DNS and LES and laboratory and field experiments, denoted by the following symbols: ∗ SHEBA field experiment (Grachev et al. 2007), △ LES (Zilitinkevich et al. 2007), ◁ DNS (Stretch et al. 2010), □ Carbon in the Mountains Experiment (Mahrt and Vickers 2005), ▽ Cooperative Atmosphere–Surface Exchange Study (Poulos et al. 2002), and ○ wind tunnel (Ohya 2001).

result of the decrease in A_z (see Fig. 4). This enhancement of e_p/e_w with increasing R_f implies that, at a given e_w, turbulence can ''store'' much more TPE, which can be later used to reenergize the turbulence, thereby preserving the turbulent state. Figure 3a also suggests that the rapid decrease in A_z within the EFB model results in $\partial(e_p/e_w)/\partial R_f \to \infty$ in the vicinity of $R_f \to R_{\rm fm}$. This finding indicates that, as $R_f \to R_{\rm fm}$, the self-preservation mechanism may be amplified in the EFB model or underestimated by the MY and CSB models. Figure 3b shows the ratio e_p/e $(=A_z e_p/e_w)$ as a function of R_i. The EFB model predicts the ratio of e_p/e to be lower than those from the MY model because of the stronger decrease of A_z with increasing R_i (see Fig. 4). Again, since a parameterization for A_z is needed to convert e_p/e_w to e_p/e in the CSB model, two cases with different A_z parameterizations are shown in Fig. 3b. The significant differences between these two cases, as well as the differences between the three models, highlight the importance of A_z in controlling the self-preservation mechanism.

The wind tunnel data shown in Fig. 3b suggest that the EFB model best captures the e_p/e trend, but it should be pointed out that the EFB model used the same data for calibration. Also none of the models captures the large-eddy simulation (LES) results, and hence it is difficulty to rank the performance of three models based on these limited data. Recent direct numerical simulation (DNS) results suggest that turbulence did laminarize at large R_i (i.e., as $R_f \to R_{\rm fm}$), hinting that the self-preservation mechanism was insufficient to maintain the turbulent state (Katul et al. 2014). However, the Reynolds numbers in those DNS runs were insufficiently large to offer definitive statements. Field experiments have reported the self-preservation of turbulence (Mauritsen and Svensson 2007) for large $R_i > 0.25$ (maintaining finite velocity variances). They also have shown A_z tends to decrease with increasing R_i, though the scatter appears to preclude a general form across experiments. As also shown in Fig. 4 here, some experiments exhibited minor variations in A_z with increasing R_i (commensurate to those in the modified MY model), while others showed large variations in A_z (commensurate to those specified in the EFB).

The significance of vertical anisotropy A_z and the fact that A_z largely explains the structural differences between these models (especially between the EFB and CSB models) even for idealized surface layer conditions calls for more studies. At present, variations in A_z with increasing R_i remain uncertain because of the large scatter in data (see Fig. 4) as well as some inconsistency between experiments and LES results (Zilitinkevich et al. 2007; Ferrero et al. 2011). Determining A_z is not as straightforward as it may appear because e can be impacted by nonstationary and large-scale motions, which are not fully accounted for in the three models. Last, the connection between τ^2/e_w^2 (and e_p/e_w) and A_z with increasing R_i requires further consideration. It is noted that many field experiments (Kaimal 1973), including some experiments in the roughness sublayer above tall forests (Juang et al. 2008), suggest that τ^2/e_w^2 does not vary appreciably with atmospheric stability while A_z varies.

4. Study limitations

When comparing model results to field experiments, the work here made the following assumptions about the state of atmospheric-surface-layer turbulence applicable to all three models: stationary and planar homogeneous flows at sufficiently large Reynolds numbers under mildly to moderately stable conditions and with no mean subsidence. Field experiments rarely fit such ''niceties'' and often include effects of surface heterogeneity and submeso meandering motions, as mentioned earlier. In addition, as R_i increases (i.e., as A_z reduces), turbulence may become nonstationary and globally intermittent and admit gravity waves that are not considered in models but may well exist in data from field experiments. The CSB and MY models implicitly assume that the Ozmidov length scale remains larger than z so that z restricts the size of eddies attached to the

wall, which need not be the case under strongly stable conditions (Li et al. 2016). The CSB model assumes that z describes the transition from the production range to the inertial subrange, while the MY assumes that the master length scale is proportional to z. Both assumptions may not hold for very large R_i. The model–model and model–data comparisons are all restricted to cases when $R_f < 1$. A number of field experiments (e.g., SHEBA used here) did report $R_f > 1$, and these cases cannot be handled by all three models without additional information or terms in the budget equations. Last, all three models assume Reynolds number independence in closure constants or model parameters, which is only valid for flows with very large Reynolds numbers. The CSB model makes this assumption explicit by considering the spectral separation between the Kolmogorov microscale η and z to span orders of magnitude. This assumption allows the inertial subrange to extend to very large k without a viscous cutoff operating at the crossover from inertial to η or bottleneck effects (Katul et al. 2015) arising in the vicinity of $k\eta \approx 0.1$. Clearly, field experiments may not satisfy such idealization and introduce Reynolds number dependencies that simply cannot be explained by the current models. These topics are deemed appropriate for future research.

5. Summary and discussion

Two recently proposed models for stably stratified turbulent flows—namely, the Energy- and Flux-Budget (EFB) model and the Cospectral Budget (CSB) model—are compared for stationary and planar homogeneous atmospheric surface layer flows using the widely used MY model as a reference. This comparison is motivated by a recent study (Li et al. 2015b) reporting acceptable agreement between EFB and CSB models for turbulent Prandtl numbers under stable conditions. Here, many other aspects of the two models are considered and compared against the classical MY model and revisions to it.

The EFB model is developed in physical space while the CSB model is formulated in wavenumber space and then integrated across all wavenumbers to arrive at macroscopic results in physical space. The two models generate comparable results in terms of R_f–R_i and Pr_t–R_i relations and the decay of normalized heat flux with increasing R_i. Both models predict an increasing trend in the turbulent Prandtl number with increasing R_i. The flux Richardson number attains saturation at sufficiently large R_i in both models. Both models allow turbulence to persist at any given R_i and thus are not limited by a critical gradient Richardson number, thereby differing from the conventional MY model, which predicts a critical gradient Richardson number beyond which turbulent momentum and heat fluxes vanish. A minor modification to the MY model suggests that the longitudinal turbulent heat flux effects on the momentum flux are responsible for this particular difference between the original MY model and the EFB or CSB models. After revising one constant in the MY model that effectively terminates the effects of the longitudinal heat flux on the momentum flux, we find that the MY model can encompass any gradient Richardson number and produce results similar to the EFB and CSB models. However, such a modification yields a relatively flat (and slightly increasing) trend for the momentum flux normalized by the turbulent kinetic energy (TKE) with increasing R_i, which is inconsistent with observations.

The EFB and MY models consider vertical anisotropy in turbulent kinetic energy (A_z), which is not needed in the CSB model, given its reliance on the spectrum of the vertical velocity. When the parameterization for A_z from EFB is used in the CSB model, the two models yield comparable results in terms of the decay of momentum flux normalized by the TKE with increasing R_i. However, the two models are still vastly different in representing the ''self preservation'' mechanism of turbulence. The CSB model predicts a linear increase in the ratio of turbulent potential energy and turbulent kinetic energy in the vertical direction (e_p/e_w) with increasing flux Richardson number (when $R_f < R_{\mathrm{fm}} = 0.25$); however, the EFB and MY models show that this increase is nonlinear because of A_z, especially in the EFB model when R_f approaches R_{fm}. The connection between the reduction in A_z and the rapid increase in e_p/e_w with increasing R_f is the main mechanism responsible for the strong self-preservation of turbulence as $R_f \to R_{\mathrm{fm}}$ in the EFB model. While the feedback responsible for such self-preservation also exists in the CSB and MY models, it is much weaker in the range of $0.1 < R_f < 0.25$ when compared to the EFB model. The data for e_p/e and A_z are too scattered to definitively distinguish the performance of different models.

All three models examined here do not consider intermittent turbulence, which tends to occur under very stable conditions (Sun et al. 2002, 2004; Ohya et al. 2008; He and Basu 2015), despite the fact that some of them, such as the MY model, have been used in operational models for many years. Ad hoc corrections are often used in turbulence closures to avoid the complete degeneration of turbulence under strongly stable conditions in weather and climate models (Sandu et al. 2013). In the intermittent turbulence regime, the Reynolds averaging used in the MY and EFB models and the assumption of large-scale separation between the size of

energy-carrying and flux-transporting eddies and the Kolmogorov microscale in the CSB model become questionable, while the effects of surface heterogeneity and gravity waves become significant. In addition, the idealized spectral shapes used in the CSB model might collapse under strongly stable conditions. When $R_f > 0.11$, there is now experimental evidence to support that the vertical velocity spectrum begins to deviate from its idealized two-regime shape assumed by the CSB model (Li et al. 2015a). The SHEBA long-term experiment also shows that, when $R_f > 0.2$–0.25, the Kolmogorov scaling no longer holds in vertical velocity and temperature spectra (Grachev et al. 2013). A consequence of these deviations in spectral shapes is that the CSB model, as compared to the EFB model, is unable to account for the additional enhancement of TPE storage at a given e_w. However, if the shapes of these spectral deviations are known, they can still be included in the CSB model.

Finally, it is stressed again that a direct comparison between these models has implications for future developments of stably stratified flow theories. It shows a direct connection between ordinary turbulence closure schemes and spectral shapes, thereby providing new ways to estimate empirical constants used in ordinary turbulence closure schemes. A few examples [Eqs. (26) and (27)] illustrating how different constants in different models can be connected are featured. The linkages between the energy distributions of turbulent eddies (both kinetic and potential) encoded in the vertical velocity and air temperature spectra and macroscopic relations of the mean flow, such as the Pr_t–R_i relation, may offer new perspectives as to when dimensional considerations and similarity theories (and hence turbulence closure schemes based on dimensional considerations and similarity theories) are expected to hold. Under strongly stable conditions, the idealized spectral shapes of vertical velocity and temperature are found to no longer follow their idealized shape, which may explain why similarity theories work reasonably for moderately stable but not very stable atmospheric flows (Grachev et al. 2013; Li et al. 2015a).

Acknowledgments. GK acknowledges support from the U.S. National Science Foundation (NSF-EAR-1344703, DGE-1068871) and the U.S. Department of Energy (DOE) through the Office of Biological and Environmental Research (BER) Terrestrial Carbon Processes (TCP) program (DE-SC0006967 and DE-SC0011461). SZ acknowledges support from the Academy of Finland Project ABBA 280700 (2014–17); the Russian Ministry of Education and Science Mega-Grant 11.G34.31.0048 (2011–15); and the Russian Science Foundation Projects 15-17-20009 (2015–18) and 15-17-30009 (2015–18).

APPENDIX

Governing Equations and Turbulence Closures

For model comparison purposes, the atmospheric surface layer flow is assumed to be stationary, planar homogeneous, lacking any subsidence so that $\overline{w} = 0$, and with turbulence sufficiently developed so that the air viscosity ν is much smaller than K_m and the molecular diffusivity of heat D_m is much smaller than K_T, where K_m and K_T are the turbulent diffusivities of momentum and heat, respectively. The molecular Prandtl number of air is defined as $\mathrm{Pr}_m = \nu/D_m \approx 0.72$, which is different from the turbulent Prandtl number $\mathrm{Pr}_t = K_m/K_T$ that varies with density stratification. Moreover, the Boussinesq approximation for density fluctuations in the advective acceleration terms is assumed to hold throughout. These simplifications result in $d\overline{u'w'}/dz = 0$ and $d\overline{w'\theta'}/dz = 0$ when applied to the mean momentum and heat budgets. These simplifications also result in the following expressions when applied to the governing equations describing the momentum- and heat-flux budgets (Stull 1988):

$$\frac{\partial \overline{u'w'}}{\partial t} = 0 = -\overline{w'w'}S - \frac{\partial \overline{w'w'u'}}{\partial z} - \frac{1}{\rho}\frac{\partial \overline{u'p'}}{\partial z} + \left(\overline{\frac{p'}{\rho}\frac{\partial u'}{\partial z}} + \overline{\frac{p'}{\rho}\frac{\partial w'}{\partial x}}\right) + \beta\overline{u'\theta'} - 2\nu\overline{\frac{\partial u'}{\partial z}\frac{\partial w'}{\partial z}}, \quad \text{and} \tag{A1}$$

$$\frac{\partial \overline{w'\theta'}}{\partial t} = 0 = -\overline{w'w'}\Gamma - \frac{\partial \overline{w'w'\theta'}}{\partial z} - \frac{1}{\rho}\frac{\partial \overline{\theta'p'}}{\partial z} + \overline{\frac{p'}{\rho}\frac{\partial \theta'}{\partial z}} + \beta\overline{\theta'\theta'} - (\nu + D_m)\overline{\frac{\partial w'}{\partial z}\frac{\partial T'}{\partial z}}, \tag{A2}$$

where p' are deviations in air pressure from the hydrostatic state. The terms on the left-hand side of the equations represent temporal changes in turbulent fluxes. The terms on the right-hand side represent (in order): production terms due to the presence of mean velocity and temperature gradients, turbulent transport terms, pressure transport terms, pressure redistribution terms, buoyancy terms arising from thermal stratification in the atmosphere, and molecular destruction terms. Both pressure transport and pressure redistribution terms arise because of turbulent interactions between pressure and velocity or temperature.

Evident from Eqs. (A1) and (A2) is the need to derive governing equations for $\overline{w'w'}$, $\overline{\theta'\theta'}$, and $\overline{u'\theta'}$ to close the turbulent flux budgets. These are given by

$$\frac{\partial \overline{w'w'}}{\partial t} = 0 = 2\beta \overline{w'\theta'} - \frac{\partial \overline{w'w'w'}}{\partial z} - \frac{2}{\rho}\frac{\partial \overline{w'p'}}{\partial z} + 2\frac{\overline{p'}}{\rho}\frac{\partial w'}{\partial z} - 2\nu\overline{\left(\frac{\partial w'}{\partial z}\right)^2}, \quad \text{(A3)}$$

$$\frac{\partial \overline{\theta'\theta'}}{\partial t} = 0 = -2\overline{w'\theta'}\Gamma - \frac{\partial \overline{w'\theta'\theta'}}{\partial z} - 2D_m\overline{\left(\frac{\partial \theta'}{\partial z}\right)^2}, \quad \text{and} \quad \text{(A4)}$$

$$\frac{\partial \overline{u'\theta'}}{\partial t} = 0 = -(\overline{u'w'}\Gamma + \overline{w'\theta'}S) - \frac{\partial \overline{u'w'\theta'}}{\partial z} + \frac{\overline{p'}}{\rho}\frac{\partial \theta'}{\partial x} - (\nu + D_m)\frac{\partial u'}{\partial z}\frac{\partial \theta'}{\partial z}. \quad \text{(A5)}$$

Similarly, the terms on the right-hand side of the equations represent (in order): production terms due to the presence of mean gradients (i.e., S and Γ) or due to buoyancy for $\overline{w'w'}$, turbulent transport terms, pressure-decorrelationterms due to interactions between pressure and velocity and between pressure and temperature (that are absent for $\overline{\theta'\theta'}$), and molecular destruction terms.

Given that $\overline{u'u'}$ and $\overline{v'v'}$ do not affect the turbulent momentum and heat fluxes, they do not need to be included when solving these budget equations. As shown later, the CSB model only requires the vertical component of TKE (i.e., the vertical velocity variance $\overline{w'w'}$) and does not require the total TKE. However, for completeness, second-order closure schemes, including the MY model and the EFB model, typically consider the total TKE equation or two separate equations for $\overline{u'u'}$ and $\overline{v'v'}$. Here, only the total TKE (e) equation is presented as follows:

$$\frac{\partial \overline{e}}{\partial t} = 0 = -\overline{u'w'}S + \beta\overline{w'\theta'} - \frac{\partial \overline{w'e}}{\partial z} - \frac{1}{\rho}\frac{\partial \overline{w'p'}}{\partial z} - \varepsilon, \quad \text{(A6)}$$

where ε is the mean TKE dissipation rate.

a. The MY model

For over four decades now, the MY model and its many variants remain widely used in geophysical turbulence parameterization. The MY model neglects the pressure transport terms (e.g., $\partial\overline{u'p'}/\partial z$ and $\partial\overline{\theta'p'}/\partial z$) and the dissipation terms in the governing equations describing turbulent fluxes. The key parameterization used in the MY model is the Rotta scheme (Rotta 1951a,b) for pressure redistribution terms, {e.g., $[\overline{(p'/\rho)(\partial u'/\partial z)} + \overline{(p'/\rho)(\partial w'/\partial x)}]$ and $\overline{(p'/\rho)(\partial\theta'/\partial z)}$}, which involves one (Mellor 1973) or three (Yamada 1975) or even more (Nakanish 2001) constants depending on the complexity of Rotta closure. In addition, the MY model employs four length scales (two are relaxation length scales in the Rotta model and two are dissipative length scales for parameterizing the dissipation rates of variances), all of which are assumed to be proportional to the so-called master length scale. To match expectations from a neutral atmospheric surface layer, the master length scale is set to be κz, where $\kappa = 0.4$ is the von Kármán constant and z is the distance from the boundary or zero-plane displacement in the case of tall vegetated canopies. As a result, the MY model requires five (Mellor 1973) or seven (Yamada 1975) empirical constants, which are usually obtained by fitting to experiments.

The MY model includes a hierarchy of closure schemes, and the level-2 scheme, which is discussed here, further neglects the turbulent transport terms in Eqs. (A1)–(A6). Under such conditions, the set of equations can be solved analytically, as shown in Mellor (1973) and Yamada (1975), which is not repeated here.

b. The EFB model

The main differences between the EFB model and the MY model are as follows: 1) The $\overline{u'\theta'}$ equation [Eq. (A5)] is not explicitly solved for, though the $\overline{u'\theta'}$ term in the momentum flux equation [Eq. (A1)] is lumped with the pressure redistribution term. 2) The $\overline{w'w'}$ equation [Eq. (A3)] is not solved; instead, the total TKE equation is solved, and the stability dependence of the vertical anisotropy is parameterized, which requires an extra constant (C_o^{efb}). 3) The maximum flux Richardson number R_{fm} needs to be empirically determined and adds to the list of constants in the EFB model. 4) The parameterization for pressure decorrelations is simpler than the Rotta version used in the MY model. The EFB parameterization is based on a "return to isotropy" concept and only requires one empirical constant (C_r^{efb}), as compared to three constants in Yamada (1975). 5) The dissipation length scale in the TKE equation is assumed to be identical to the master length scale instead of being proportional to the master length scale in the MY model (thus reducing a constant), but the master length scale in the EFB model is stability dependent and requires a constant (C_Ω^{efb}) in its parameterization. As a result, the EFB model, when not considering $\overline{u'u'}$ and $\overline{v'v'}$, also requires the specification of seven basic constants in total for atmospheric surface layer flows. These constants have been obtained through fitting to a wide range of experiments and numerical simulations.

c. The CSB model

Unlike ordinary turbulence closure schemes, such as the MY and EFB models, the CSB approach solves the cospectral budgets for momentum and heat fluxes using idealized spectral shapes for the vertical velocity and air temperature, which are principally based on the Kolmogorov (1941a,b) and the Kolmogorov–Obukhov–Corrsin (Corrsin 1951; Obukhov 1968) scaling, respectively,

at small scales. For eddies larger than those associated with the inertial subrange, it is assumed that boundary effects randomize the energy distribution across wavenumbers and the spectra are approximated by white noise. This shape appears to be supported by field experiments over relatively homogeneous surfaces in the atmospheric surface layer, provided the maximum flux Richardson number R_{fm} is not exceeded (Grachev et al. 2013; Li et al. 2015a). Based on these two regimes delineating the spectral shapes of vertical velocity and air temperature, the cospectra are then integrated over the wavenumber space to arrive at macroscopic results in the physical space. A variety of expressions can be derived depending on the idealized spectral shapes for vertical velocity and air temperature, the role of flux transfer terms, similarity in the Rotta and isotropization of production constants, and the form of the wavenumber-dependent relaxation time scales along with their scalewise similarity for momentum and heat transfer (Katul et al. 2013a, 2014; Li et al. 2015a,b). In this study, the results from Katul et al. (2014) are presented. It is noted that, when R_i increases, these expressions appear robust to the assumed shapes in the low k range of the vertical velocity and air temperature spectra, provided similarity (flat or otherwise) is maintained and the inertial subrange scaling (i.e., $k^{-5/3}$) prevails at large k (Katul et al. 2014). The similarity in spectral shapes at low k between the vertical velocity and air temperature spectra for well-developed turbulence may be a plausible assumption at large R_i given the active role of temperature in shaping the vertical velocity fluctuations, and this appears to be supported by DNS results (Katul et al. 2014).

REFERENCES

Anderson, P. S., 2009: Measurement of Prandtl number as a function of Richardson number avoiding self-correlation. *Bound.-Layer Meteor.*, **131**, 345–362, doi:10.1007/s10546-009-9376-4.

Andren, A., 1995: The structure of stably stratified atmospheric boundary layers: A large-eddy simulation study. *Quart. J. Roy. Meteor. Soc.*, **121**, 961–985, doi:10.1002/qj.49712152502.

Basu, S., F. Porté-Agel, E. Foufoula-Georgiou, J.-F. Vinuesa, and M. Pahlow, 2006: Revisiting the local scaling hypothesis in stably stratified atmospheric boundary-layer turbulence: An integration of field and laboratory measurements with large-eddy simulations. *Bound.-Layer Meteor.*, **119**, 473–500, doi:10.1007/s10546-005-9036-2.

——, A. Ruiz-Columbié, J. Phillipson, and S. Harshan, 2010: Local scaling characteristics of Antarctic surface layer turbulence. *Cryosphere*, **4**, 325–331, doi:10.5194/tc-4-325-2010.

Canuto, V. M., Y. Cheng, A. Howard, and I. Isau, 2008: Stably stratified flows: A model with no Ri(cr). *J. Atmos. Sci.*, **65**, 2437–2447, doi:10.1175/2007JAS2470.1.

Cava, D., U. Giostra, M. Siqueira, and G. Katul, 2004: Organised motion and radiative perturbations in the nocturnal canopy sublayer above an even-aged pine forest. *Bound.-Layer Meteor.*, **112**, 129–157, doi:10.1023/B:BOUN.0000020160.28184.a0.

——, ——, and G. Katul, 2015: Characteristics of gravity waves over an Antarctic ice sheet during an austral summer. *Atmosphere*, **6**, 1271–1289, doi:10.3390/atmos6091271.

Cheng, Y., V. Canuto, and A. Howard, 2002: An improved model for the turbulent PBL. *J. Atmos. Sci.*, **59**, 1550–1565, doi:10.1175/1520-0469(2002)059<1550:AIMFTT>2.0.CO;2.

Chung, D., and G. Matheou, 2012: Direct numerical simulation of stationary homogeneous stratified sheared turbulence. *J. Fluid Mech.*, **696**, 434–467, doi:10.1017/jfm.2012.59.

Corrsin, S., 1951: On the spectrum of isotropic temperature fluctuations in an isotropic turbulence. *J. Appl. Phys.*, **22**, 469–473, doi:10.1063/1.1699986.

Derbyshire, S., 1999: Stable boundary-layer modeling: Established approaches and beyond. *Bound.-Layer Meteor.*, **90**, 423–446, doi:10.1023/A:1001749007836.

Esau, I., and A. A. Grachev, 2007: Turbulent Prandtl number in stably stratified atmospheric boundary layer: Intercomparison between LES and SHEBA data. *e-WindEng*, **005**, 1–17.

Fernando, H., 1991: Turbulent mixing in stratified fluids. *Annu. Rev. Fluid Mech.*, **23**, 455–493, doi:10.1146/annurev.fl.23.010191.002323.

——, and J. Weil, 2010: Whither the stable boundary layer? A shift in the research agenda. *Bull. Amer. Meteor. Soc.*, **91**, 1475–1484, doi:10.1175/2010BAMS2770.1.

Ferrero, E., L. Quan, and D. Massone, 2011: Turbulence in the stable boundary layer at higher Richardson numbers. *Bound.-Layer Meteor.*, **139**, 225–240, doi:10.1007/s10546-010-9581-1.

Galperin, B., L. Kantha, S. Hassid, and A. Rosati, 1988: A quasi-equilibrium turbulent energy model for geophysical flows. *J. Atmos. Sci.*, **45**, 55–62, doi:10.1175/1520-0469(1988)045<0055:AQETEM>2.0.CO;2.

——, S. Sukoriansky, and P. S. Anderson, 2007: On the critical Richardson number in stably stratified turbulence. *Atmos. Sci. Lett.*, **8**, 65–69, doi:10.1002/asl.153.

Gerz, T., U. Schumann, and S. Elghobashi, 1989: Direct numerical simulation of stratified homogeneous turbulent shear flows. *J. Fluid Mech.*, **200**, 563–594, doi:10.1017/S0022112089000765.

Grachev, A., E. L Andreas, C. Fairall, P. Guest, and P. G. Persson, 2007: On the turbulent Prandtl number in the stable atmospheric boundary layer. *Bound.-Layer Meteor.*, **125**, 329–341, doi:10.1007/s10546-007-9192-7.

——, ——, ——, ——, and ——, 2012: Outlier problem in evaluating similarity functions in the stable atmospheric boundary layer. *Bound.-Layer Meteor.*, **144**, 137–155, doi:10.1007/s10546-012-9714-9.

——, ——, ——, ——, and ——, 2013: The critical Richardson number and limits of applicability of local similarity theory in the stable boundary layer. *Bound.-Layer Meteor.*, **147**, 51–82, doi:10.1007/s10546-012-9771-0.

He, P., and S. Basu, 2015: Direct numerical simulation of intermittent turbulence under stably stratified conditions. *Nonlinear Processes Geophys.*, **22**, 447–471, doi:10.5194/npg-22-447-2015.

Holtslag, A. A. M., and Coauthors, 2013: Stable atmospheric boundary layers and diurnal cycles: Challenges for weather and climate models. *Bull. Amer. Meteor. Soc.*, **94**, 1691–1706, doi:10.1175/BAMS-D-11-00187.1.

Huang, J., E. Bou-Zeid, and J.-C. Golaz, 2013: Turbulence and vertical fluxes in the stable atmospheric boundary layer. Part 2: A novel mixing-length model. *J. Atmos. Sci.*, **70**, 1528–1542, doi:10.1175/JAS-D-12-0168.1.

Ishihara, T., K. Yoshida, and Y. Kaneda, 2002: Anisotropic velocity correlation spectrum at small scales in a homogeneous turbulent shear flow. *Phys. Rev. Lett.*, **88**, 154501, doi:10.1103/PhysRevLett.88.154501.

Juang, J.-Y., G. G. Katul, M. B. Siqueira, P. C. Stoy, and H. R. McCarthy, 2008: Investigating a hierarchy of Eulerian closure models for scalar transfer inside forested canopies. *Bound.-Layer Meteor.*, **128**, 1–32, doi:10.1007/s10546-008-9273-2.

Kaimal, J. C., 1973: Turbulence spectra, length scales and structure parameters in the stable surface layer. *Bound.-Layer Meteor.*, **4**, 289–309, doi:10.1007/BF02265239.

——, and J. Finnigan, 1994: *Atmospheric Boundary Layer Flows: Their Structure and Measurement*. Oxford University Press, 304 pp.

Karimpour, F., and S. Venayagamoorthy, 2014: A simple turbulence model for stably stratified wall-bounded flows. *J. Geophys. Res. Oceans*, **119**, 870–880, doi:10.1002/2013JC009332.

Katul, G. G., D. Li, M. Chamecki, and E. Bou-Zeid, 2013a: Mean scalar concentration profile in a sheared and thermally stratified atmospheric surface layer. *Phys. Rev.*, **87**, 023004, doi:10.1103/PhysRevE.87.023004.

——, A. Porporato, C. Manes, and C. Meneveau, 2013b: Co-spectrum and mean velocity in turbulent boundary layers. *Phys. Fluids*, **25**, 091702, doi:10.1063/1.4821997.

——, ——, S. Shah, and E. Bou-Zeid, 2014: Two phenomenological constants explain similarity laws in stably stratified turbulence. *Phys. Rev.*, **89**, 023007, doi:10.1103/PhysRevE.89.023007.

——, C. Manes, A. Porporato, E. Bou-Zeid, and M. Chamecki, 2015: Bottlenecks in turbulent kinetic energy spectra predicted from structure function inflections using the Von Kármán–Howarth equation. *Phys. Rev.*, **92**, 033009, doi:10.1103/PhysRevE.92.033009.

Klipp, C. L., and L. Mahrt, 2004: Flux-gradient relationship, self-correlation and intermittency in the stable boundary layer. *Quart. J. Roy. Meteor. Soc.*, **130**, 2087–2103, doi:10.1256/qj.03.161.

Kolmogorov, A., 1941a: Dissipation of energy under locally isotropic turbulence. *Dokl. Akad. Nauk SSSR*, **32**, 16–18.

——, 1941b: The local structure of turbulence in imcompressible viscous fluid for very large Reynolds numbers. *Dokl. Akad. Nauk SSSR*, **30**, 299–303.

Kosovic, B., and J. A. Curry, 2000: A large-eddy simulation study of a quasi-steady, stably stratified atmospheric boundary layer. *J. Atmos. Sci.*, **57**, 1052–1068, doi:10.1175/1520-0469(2000)057<1052:ALESSO>2.0.CO;2.

Li, D., G. G. Katul, and E. Bou-Zeid, 2015a: Turbulent energy spectra and cospectra of momentum and heat fluxes in the stable atmospheric surface layer. *Bound.-Layer Meteor.*, **157**, 1–21, doi:10.1007/s10546-015-0048-2.

——, ——, and S. S. Zilitinkevich, 2015b: Revisiting the turbulent Prandtl number in an idealized atmospheric surface layer. *J. Atmos. Sci.*, **72**, 2394–2410, doi:10.1175/JAS-D-14-0335.1.

——, S. Salesky, and T. Banerjee, 2016: Connections between the Ozmidov scale and mean velocity profile in stably stratified atmospheric surface layers. *J. Fluid Mech.*, **797**, R3, doi:10.1017/jfm.2016.311.

Mahrt, L., 1999: Stratified atmospheric boundary layers. *Bound.-Layer Meteor.*, **90**, 375–396, doi:10.1023/A:1001765727956.

——, 2009: Characteristics of submeso winds in the stable boundary layer. *Bound.-Layer Meteor.*, **130**, 1–14, doi:10.1007/s10546-008-9336-4.

——, 2014: Stably stratified atmospheric boundary layers. *Annu. Rev. Fluid Mech.*, **46**, 23–45, doi:10.1146/annurev-fluid-010313-141354.

——, and D. Vickers, 2005: Boundary-layer adjustment over small-scale changes of surface heat flux. *Bound.-Layer Meteor.*, **116**, 313–330, doi:10.1007/s10546-004-1669-z.

Mauritsen, T., and G. Svensson, 2007: Observations of stably stratified shear-driven atmospheric turbulence at low and high Richardson numbers. *J. Atmos. Sci.*, **64**, 645–655, doi:10.1175/JAS3856.1.

Mellor, G. L., 1973: Analytic prediction of the properties of stratified planetary surface layers. *J. Atmos. Sci.*, **30**, 1061–1069, doi:10.1175/1520-0469(1973)030<1061:APOTPO>2.0.CO;2.

——, and T. Yamada, 1974: A hierarchy of turbulence closure models for planetary boundary layers. *J. Atmos. Sci.*, **31**, 1791–1806, doi:10.1175/1520-0469(1974)031<1791:AHOTCM>2.0.CO;2.

——, and ——, 1982: Development of a turbulence closure model for geophysical fluid problems. *Rev. Geophys.*, **20**, 851–875, doi:10.1029/RG020i004p00851.

Miller, N. E., and R. Stoll, 2013: Surface heterogeneity effects on regional-scale fluxes in the stable boundary layer: Aerodynamic roughness length transitions. *Bound.-Layer Meteor.*, **149**, 277–301, doi:10.1007/s10546-013-9839-5.

Nakanish, M., 2001: Improvement of the Mellor–Yamada turbulence closure model based on large-eddy simulation data. *Bound.-Layer Meteor.*, **99**, 349–378, doi:10.1023/A:1018915827400.

Obukhov, A., 1968: Structure of the temperature field in turbulent flow. Defense Technical Information Center Tech. Rep. 683016, 14 pp.

Ohya, Y., 2001: Wind-tunnel study of atmospheric stable boundary layers over a rough surface. *Bound.-Layer Meteor.*, **98**, 57–82, doi:10.1023/A:1018767829067.

——, R. Nakamura, and T. Uchida, 2008: Intermittent bursting of turbulence in a stable boundary layer with low-level jet. *Bound.-Layer Meteor.*, **126**, 349–363, doi:10.1007/s10546-007-9245-y.

Pardyjak, E., P. Monti, and H. Fernando, 2002: Flux Richardson number measurements in stable atmospheric shear flows. *J. Fluid Mech.*, **459**, 307–316, doi:10.1017/S0022112002008406.

Pope, S., 2000: *Turbulent Flows*. Cambridge University Press, 771 pp.

Poulos, G. S., and Coauthors, 2002: CASES-99: A comprehensive investigation of the stable nocturnal boundary layer. *Bull. Amer. Meteor. Soc.*, **83**, 555–558, doi:10.1175/1520-0477(2002)083<0555:CACIOT>2.3.CO;2.

Rodrigo, J. S., and P. S. Anderson, 2013: Investigation of the stable atmospheric boundary layer at Halley Antarctica. *Bound.-Layer Meteor.*, **148**, 517–539, doi:10.1007/s10546-013-9831-0.

Rohr, J. J., E. C. Itsweire, K. N. Helland, and C. W. V. Atta, 1988: Growth and decay of turbulence in a stably stratified shear flow. *J. Fluid Mech.*, **195**, 77–111, doi:10.1017/S0022112088002332.

Rotta, J., 1951a: Statistical theory of nonhomogeneous turbulence—Part 1. *Z. Phys.*, **129**, 257–572.

——, 1951b: Statistical theory of nonhomogeneous turbulence—Part 2. *Z. Phys.*, **131**, 51–77.

Sandu, I., A. Beljaars, P. Bechtold, T. Mauritsen, and G. Balsamo, 2013: Why is it so difficult to represent stably stratified conditions in numerical weather prediction (NWP) models? *J. Adv. Model. Earth Syst.*, **5**, 117–133, doi:10.1002/jame.20013.

Schumann, U., and T. Gerz, 1995: Turbulent mixing in stably stratified shear flows. *J. Appl. Meteor.*, **34**, 33–48, doi:10.1175/1520-0450-34.1.33.

Shih, L., J. Koseff, J. Ferziger, and C. Rehmann, 2000: Scaling and parameterization of stratified homogeneous turbulent shear flow. *J. Fluid Mech.*, **412**, 1–20, doi:10.1017/S0022112000008405.

Sorbjan, Z., 2006: Local structure of turbulence in stably stratified boundary layers. *J. Atmos. Sci.*, **63**, 1526–1537, doi:10.1175/JAS3704.1.

——, 2010: Gradient-based scales and similarity laws in the stable boundary layer. *Quart. J. Roy. Meteor. Soc.*, **136**, 1243–1254, doi:10.1002/qj.638.

——, 2014: Modelling of the evolving stable boundary layer. *Bound.-Layer Meteor.*, **151**, 407–428, doi:10.1007/s10546-013-9893-z.

Stoll, R., and F. Porté-Agel, 2009: Surface heterogeneity effects on regional-scale fluxes in stable boundary layers: Surface temperature transitions. *J. Atmos. Sci.*, **66**, 412–431, doi:10.1175/2008JAS2668.1.

Strang, E., and H. Fernando, 2001: Entrainment and mixing in stratified shear flows. *J. Fluid Mech.*, **428**, 349–386, doi:10.1017/S0022112000002706.

Stretch, D., J. Rottman, S. Venayagamoorthy, K. K. Nomura, and C. R. Rehmann, 2010: Mixing efficiency in decaying stably stratified turbulence. *Dyn. Atmos. Oceans*, **49**, 25–36, doi:10.1016/j.dynatmoce.2008.11.002.

Stull, R. B., 1988: *An Introduction to Boundary Layer Meteorology*. Kluwer Academic, 666 pp.

Sun, J., and Coauthors, 2002: Intermittent turbulence associated with a density current passage in the stable boundary layer. *Bound.-Layer Meteor.*, **105**, 199–219, doi:10.1023/A:1019969131774.

——, and Coauthors, 2004: Atmospheric disturbances that generate intermittent turbulence in nocturnal boundary layers. *Bound.-Layer Meteor.*, **110**, 255–279, doi:10.1023/A:1026097926169.

——, and Coauthors, 2015: Review of wave–turbulence interactions in the stable atmospheric boundary layer. *Rev. Geophys.*, **53**, 956–993, doi:10.1002/2015RG000487.

Venayagamoorthy, S., and D. Stretch, 2010: On the turbulent Prandtl number in homogeneous stably stratified turbulence. *J. Fluid Mech.*, **644**, 359–369, doi:10.1017/S002211200999293X.

Webster, C., 1964: An experimental study of turbulence in a density-stratified shear flow. *Dyn. Atmos. Oceans*, **19**, 221–245, doi:10.1017/S0022112064000672.

Yamada, T., 1975: The critical Richardson number and the ratio of the eddy transport coefficients obtained from a turbulence closure model. *J. Atmos. Sci.*, **32**, 926–933, doi:10.1175/1520-0469(1975)032<0926:TCRNAT>2.0.CO;2.

Zilitinkevich, S., T. Elperin, N. Kleeorin, and I. Rogachevskii, 2007: Energy- and flux-budget (EFB) turbulence closure model for stably stratified flows. Part I: Steady-state, homogeneous regimes. *Bound.-Layer Meteor.*, **125**, 167–192, doi:10.1007/s10546-007-9189-2.

——, ——, ——, ——, I. Esau, T. Mauritsen, and M. Miles, 2008: Turbulence energetics in stably stratified geophysical flows: Strong and weak mixing regimes. *Quart. J. Roy. Meteor. Soc.*, **134**, 793–799, doi:10.1002/qj.264.

——, ——, ——, ——, and ——, 2013: A hierarchy of energy- and flux-budget (EFB) turbulence closure models for stably-stratified geophysical flows. *Bound.-Layer Meteor.*, **146**, 341–373, doi:10.1007/s10546-012-9768-8.